



Characterizations of continuous carbon fiber-reinforced composites for electromagnetic interference shielding fabricated by 3D printing

Lixian Yin¹ · Xiaoyong Tian¹ · Zhentao Shang¹ · Xin Wang¹ · Zhanghao Hou¹

Received: 28 December 2018 / Accepted: 18 March 2019 / Published online: 22 March 2019
© Springer-Verlag GmbH Germany, part of Springer Nature 2019

Abstract

With an increase in electromagnetic interference pollution, composites for electromagnetic interference shielding (EMIS) with good shielding performance and friendly processability are widely demanded. Herein, a methodology for preparing composites with controllable shielding effectiveness (SE) is proposed. Carbon fiber (CF)-reinforced polylactic acid composites were fabricated by a 3D printing process, and the SE of the composites was controlled by varying the process parameters. To systematically investigate the feasibility of the methodology, the shielding properties, processability, and mechanical properties of the composites were investigated. The results showed that the SE was controlled in the ranges of 25.1–69.9 dB, 51.1–75.6 dB, and 6.8–78.9 dB by tailoring the number of layers (2–12), hatch spacing (1.6–0.8 mm), and filling angle (90°–0°), respectively. The critical mechanism of the controllability is that the content, spatial distribution, and orientation of CFs can be facilely and digitally controlled during processing. A conformal shell with a SE of 38.5 dB was fabricated to demonstrate superior processability of a complex geometry. The maximum tensile and flexural strengths of the composites were 111.0 and 152.9 MPa, respectively, which were much larger than those of most engineering plastics. Using this methodology, an appropriate SE that is neither excessive nor deficient can be readily realized, which helps to maintain high resource utilization. Complex geometries for EMIS can be rapidly and cheaply obtained without molds, which is difficult for traditional processes. These advantages make the 3D-printed CF-reinforced composites competitive with other EMIS materials and traditional processes.

1 Introduction

With the growth of telecommunications and electronics, electromagnetic interference shielding (EMIS) is receiving increasing attention for protecting devices and people [1]. EMIS materials can minimize the signal passing through a system by reflecting or absorbing and dissipating the radiation power of electromagnetic waves. Carbon composites such as carbon fibers (CFs), graphite, carbon black, graphene, and carbon nanotubes (CNTs) have been widely used to form carbon-based EMIS composites [2–8] owing to their superior advantages over traditional metals, such as their light weights, corrosion resistances, and good processabilities. Among carbon composites, CF/polymer composites are

outstanding owing to the excellent electrical and mechanical properties of CFs, the low density and good corrosion resistance of polymers [9].

Lu et al. [10] used chopped CFs with lengths of 2–8 mm to synthesize composites and realized a shielding effectiveness (SE) of 39.2 dB at 30–1500 MHz (90 wt% CFs). Compared to short-cut fibers, continuous CFs have long conductive pathways owing to the continuity of the fibers. Hu et al. [11] fabricated carbonyl iron powder (CIP)-reinforced CF felt/epoxy resin (EP) composites by a vacuum bag molding process, obtaining a maximum SE of 53.9 dB. Micheli et al. [12] integrated layers of woven Kevlar and carbon fabric within a polymeric matrix by a hot-pressing process, obtaining a SE of 80 dB. They demonstrated the good EMIS properties of continuous CF composites. However, the processes they used require molds, which are costly and time intensive to prepare. Composites with customized shielding properties or complex geometries are hard to prepare, so they cannot meet the high demand for customization of EMIS materials.

Recently, 3D printing technologies have attracted much attention for their high efficiencies, low costs, and superior

✉ Xiaoyong Tian
leoxyt@mail.xjtu.edu.cn

¹ State Key Laboratory of Manufacturing Systems Engineering, Rapid Manufacturing Engineering Technology Research Center of Shaanxi Province, Xi'an Jiaotong University, Xianning West Road 28, Xi'an 710049, China

abilities to fabricate complex structures without molds [13–17]. Some researchers have demonstrated the feasibility of using 3D printing technologies to fabricate EMIS carbon composites. Chizari et al. [18] used solvent-cast 3D printing to fabricate a CNT/poly(lactic acid) (PLA) nanocomposite for EMIS application and tested the influence of different geometries on the SE. Paddubskaya et al. [19, 20] fabricated nanocarbon periodic sandwich structures by a dual fused deposition modeling (FDM) process. However, as a potential reinforcement for EMIS, continuous CFs were not used as printing materials until a 3D printing process for continuous-fiber-reinforced composites was proposed by our research group [21, 22]. Because the distribution of conductive material in a polymeric composite usually affects the SE, it was deduced that the SE of continuous-CF-reinforced composites may be readily controlled in the 3D printing process. A controlled SE may help provide the composite with an appropriate SE that is neither excessive nor deficient, which is significant for maintaining high material utilization and processing efficiency. Additionally, considering the inherent advantages of 3D printing, such as the ability to fabricate conformal structures without molds [21], 3D-printed continuous-CF-reinforced composites may hold great potential for use in EMIS applications.

Moreover, owing to the superior mechanical properties of CFs, CF-reinforced composites may be multifunctional, providing both mechanical load-bearing capability and microwave shielding. Recently, the mechanical properties of 3D printed continuous-CF-reinforced thermal plastics have been reported. Klift et al. [23], Hao et al. [24] and Tian et al. [21] printed continuous-CF-reinforced composites, obtaining tensile strength of 464.4 MPa and 792.8 MPa, flexural strength of 335 MPa, respectively. Li et al. [25] developed modified-continuous-CF-reinforced composites, obtaining tensile strength and flexural strengths of 91 MPa and 156 MPa, respectively. Yang et al. [26] developed continuous-CF-reinforced acrylonitrile-butadiene-styrene (ABS) composites, obtaining tensile and flexural strength of 147 MPa and 127 MPa, respectively. The mechanical properties of all the aforementioned composites are better than most 3D-printed pure engineering plastics such as polystyrene (PS), polycarbonate (PC), polyamide (PA), polypropylene (PP), and ABS, which have tensile strengths of 19.5 MPa, 43.0 MPa, 18.0 MPa, 2.45 MPa and 50 MPa, respectively [26–30]. Besides, the mechanical properties of the aforementioned 3D-printed continuous-CF-reinforced composites are also better than those of most 3D printed short-CF-reinforced composites, which usually have tensile strengths smaller than 70 MPa [31–36].

In this work, a methodology for controlling the shielding properties of composites by tailoring three process parameters in the 3D printing process (the filling angle, number of layers, and hatch spacing) is proposed. To investigate the

feasibility of the methodology, three groups of CF composites with various filling angles, number of layers, and hatch spacings are prepared and measured. Additionally, two critical factors affecting the practical application of EMIS materials, the processability and mechanical properties of the composites are also investigated. A shielding shell is fabricated to demonstrate the feasibility of the process for manufacturing complex shielding structures. The flexural and tensile strengths of the composites are measured to evaluate the mechanical properties of the composites.

2 Process

2.1 Mechanism and facility

The 3D printing facilities used in this research are shown in Fig. 1a, b. The FDM-based 3D printer (COMBOT-I, ShaanXi Fibertech Technology Development Co. Ltd., China) in Fig. 1a was used to fabricate cuboid samples. The facility comprises an extrusion head, a platform, X–Y–Z motion mechanisms, and a control system [21, 22]. The modified 3D printing robot in Fig. 1b employed a six-degree-of-freedom robot arm (MITSUBISHI RV-7F-1Q-S11) as the motion mechanism [37]. The robot can fabricate complex structures such as conformal structures.

A schematic diagram of the process is shown in Fig. 1c. The resin filament is continuously fed into the heating head, heated to a semiliquid state (heating temperature: 210 °C), and transported into the nozzle (diameter: 1.5 mm). At the same time, the CF passes through the inner channel of the extrusion head and reaches the nozzle. Thus, the CF is infiltrated into and coated by the molten plastic in the nozzle. Owing to the pressure from the continuously fed plastic filament, the impregnated composites can be extruded from the nozzle. As the extruded filament reaches the platform, it rapidly solidifies and adheres to the previous layer. A photograph of the specimens being printed is shown in Fig. 1d. White regions in the printing area are PLA, and black regions are CF.

2.2 Processing advantages

Compared to CF-reinforced composites fabricated by conventional CF lamination processes, the 3D-printed CF composites have several advantages. First, no mold is required in the 3D printing process, and the process conditions are mild, which reduces the time required and cost. In contrast, the composites in previous works [12, 38] were fabricated by hot-press molding, which requires molds and high pressure. Second, complicated structures, such as hollow or conformal structures, can be easily fabricated by 3D printing. Third, integrated manufacturing of large components can be realized by 3D printing

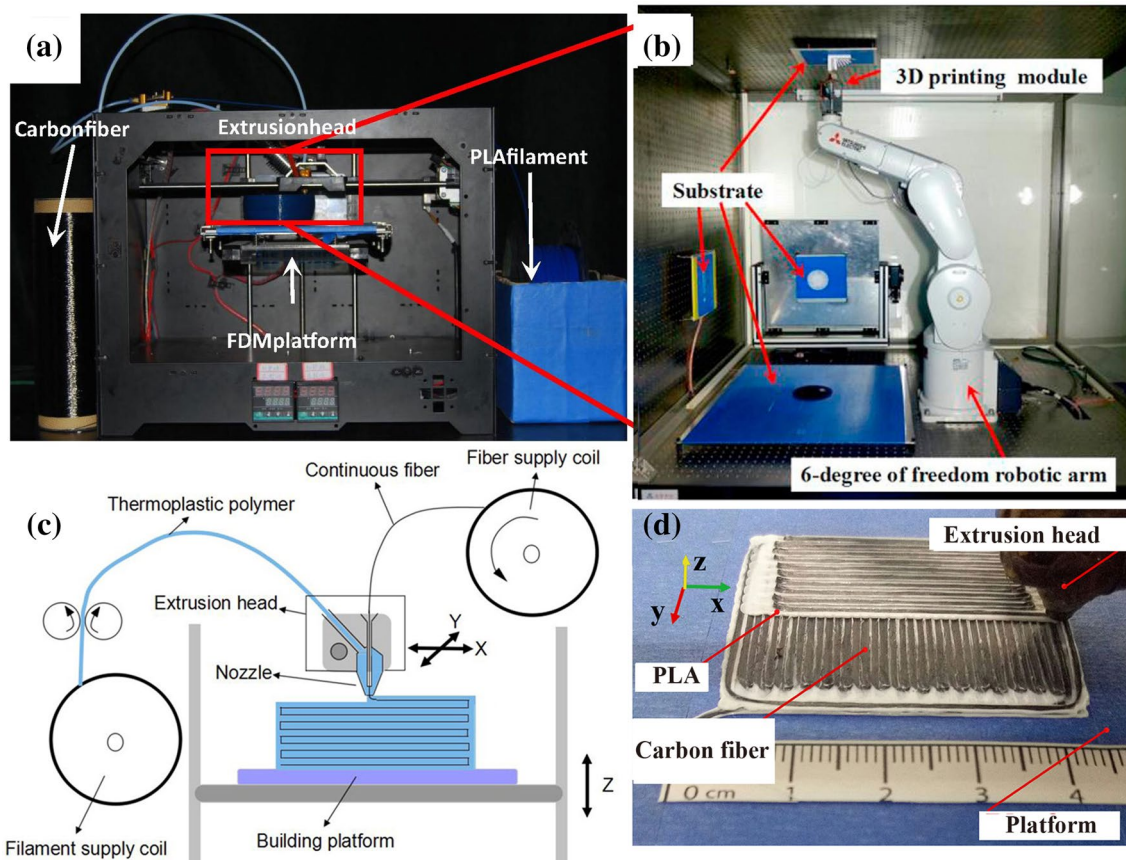


Fig. 1 Photographs of **a** FDM-based 3D printer and **b** 3D printing robot, **c** schematic diagram of the 3D printing process [37], and **d** photograph of specimens being printed

techniques with a 3D printing robot; thus, assembly is not necessary. These processing advantages help keep the composites competitive with other EMIS materials.

Additionally, various matrix materials are available for the 3D printing. Thermoplastic materials such as PLA, ABS, PC, PP, PS, PA, and polyetheretherketone (PEEK) can be used as matrix materials. It is easy to prepare shielding materials with other functions. For example, to manufacture shielding materials with high-temperature resistance, PEEK could be used as the matrix material because of its high thermal deformation temperature (above 300 °C). To manufacture shielding materials with high-impact resistance, PC can be used as the matrix. To manufacture environmentally friendly shielding materials, PLA can be used for its degradability. In this work, PLA was used as the matrix material.

3 Experimental

3.1 Materials

PLA filaments from Flashforge Co. Ltd. (China) were used as the thermoplastic matrix. The real part of complex dielectric permittivity and dielectric loss tangent of PLA are 2.6 and 0.02, respectively. The tensile and flexural strength of the 3D-printed PLA are 44 and 84 MPa, respectively. CFs (T300-1K, 1000 filaments in a bundle) from TENAX-J Corp. in China were used as the reinforcement. The density and conductivity of the CFs are 1.8 g/cm³ and 5.9×10^4 S/m, respectively.

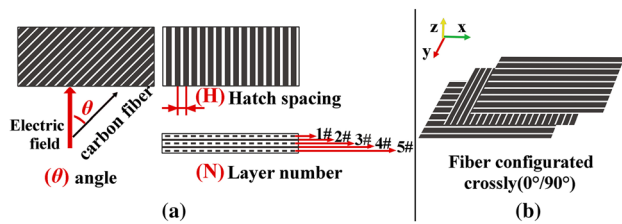


Fig. 2 **a** Schematic diagrams of process parameters and CF configurations including filling angle θ , hatch spacing H , and number of layers N . **b** CFs configured so as to cross each other, with filling angles θ of 0° and 90° in adjacent layers

3.2 Procedures

There are three key parameters for 3D printing of continuous-fiber-reinforced composites, as shown in Fig. 2a. N is the number of deposited layers, which affects the total quantity of CFs and total thickness of the sample. The hatch spacing H is the central distance between two adjacent deposited composite lines, which affects the content and spatial distribution of the CFs. The filling angle θ is the angle between the CFs and the Y -direction of the motion mechanisms, which affects the orientation of the CFs. The direction of the electric field (E field) in the measurement described in Sect. 4.2 is also in the Y -direction. Hence, the content, spatial distribution, and orientation of the CFs can be facily and digitally controlled during processing.

First, to investigate the feasibility of controlling the SE by tailoring the process parameters, N , H , and θ , three groups of cuboid samples were prepared and measured. The parameter matrix of the samples is shown in Table 1. Group 1 consisted of composites with different N values (2, 4, 6, 8, 10, and 12) to test the effect of N on the SE. Group 2 consisted of composites with different H values (0.8, 1.0, 1.2, 1.4, and 1.6 mm) to test the effect of H on the SE. Group 3 consisted of composites with different θ values (0° , 30° , 45° , 60° , 90°) to test the effect of CF orientation on the SE. In groups 1 and 2, the CFs were configured crossly with θ values of 0° and 90° in adjacent layers ($\theta = 0^\circ/90^\circ$), as shown in Fig. 2b, to decrease the sensitivity of the SE to the external electric field.

Then to demonstrate that continuous-CF-reinforced EMIS composites with complex geometries can be fabricated by

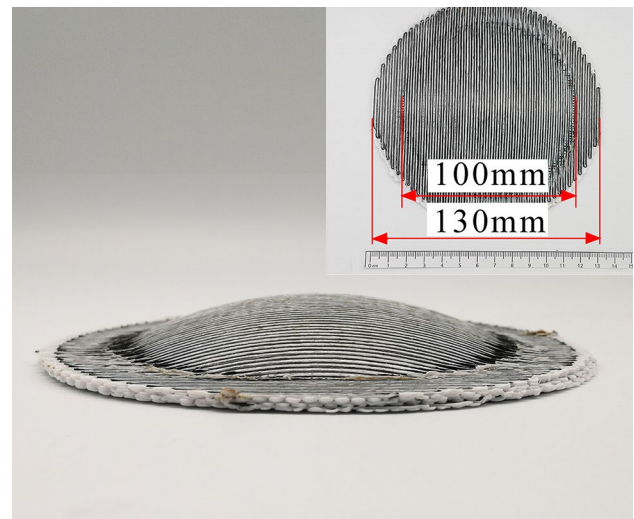


Fig. 3 Photograph of the CF composite shells fabricated by the 3D printing process

this process, a hat-like shell was fabricated by the 3D printing robot. Top and perspective views of the shell are shown in Fig. 3. The diameters of the brim and crown of the shell were 130 and 100 mm, respectively. The total height was 15 mm. H and N were 1.2 mm and 4, respectively. θ was $0^\circ/90^\circ$, as described above. The SE was measured.

Finally, the flexural and tensile properties of the composites prepared by the proposed methodology were measured to investigate their mechanical behavior. H was 1.2 mm, and θ was $0^\circ/90^\circ$. The N values of the samples used for tensile and flexural testing were 4 and 8, respectively.

3.3 Characterizations

The morphology and microstructure of the 3D-printed composites were characterized by field emission scanning electron microscopy (FE-SEM, SU-8010, Hitachi, Japan). The SE of the samples in groups 1, 2, and 3 was measured by a vector network analyzer (E8363B, Agilent, USA) and a waveguide (WR90) according to standard IEEE STD 299-2006. The cuboid samples had dimensions of $22.9 \times 10.2 \times 5 \text{ mm}^3$. The SE of the shell was measured by a vector network analyzer (E8363B, Agilent, USA) and a pair of horn antennas according to standard

Table 1 Parameter matrix of the three groups of composites

Group	Target parameter	Range	Other parameters	CF volume content
1	Number of layers N	2, 4, 6, 8, 10, 12	$\theta = 0^\circ/90^\circ$, $H = 1.2 \text{ mm}$	6.41%
2	Hatch spacing H (mm)	0.8, 1.0, 1.2, 1.4, 1.6	$\theta = 0^\circ/90^\circ$, $N = 10$	9.62%, 7.69%, 6.41%, 5.50%, 4.81%
3	Angle θ (degree)	0° , 30° , 45° , 60° , 90°	$N = 10$, $H = 1.2 \text{ mm}$	6.41%

GJB 6190-2008. The tensile and flexural strength were measured by a universal testing machine (PLD-5kN, Letry Corp., China). The dimensions of the samples for tensile and flexural testing were $200 \times 12.5 \times 2 \text{ mm}^3$ and $80 \times 10 \times 4 \text{ mm}^3$, respectively. All samples were tested at a load rate of 1 mm/min. The reported results are averages of the values of five samples.

When a wave is incident on a shielding material, there is a direct reflection at the surface of the shielding material because of the impedance mismatch between the shielding material and air. On the other hand, some waves successfully enter the shielding materials and are reflected again and again between the two interfaces of the shielding materials. Some waves are absorbed through the electric and polarization loss and so on. The SE is described as follows:

$$SE = SE_a + SE_r + SE_m, \quad (1)$$

where SE_a , SE_r , and SE_m are the shielding efficiency resulting from absorption, direct reflection at the surface, and multiple reflection between the two interfaces of the shielding materials, respectively.

When SE_a is higher than 15 dB, SE_m can be ignored [39], and the SE can be expressed as follows:

$$SE = SE_a + SE_r. \quad (2)$$

The transmission coefficient (S_{21}) and the reflection coefficient (S_{11}) measured by the vector network analyzer were used to calculate SE_r and SE_a as follows:

$$SE_r = -10 \log(1 - |S_{11}|^2), \quad (3)$$

$$SE_a = -10 \log[|S_{21}|^2 / (1 - |S_{11}|^2)]. \quad (4)$$

The average SE was calculated by averaging 201 SE values at different frequency points.

4 Results and discussion

4.1 Morphology and micro-structure of composites

Figure 4 shows an optical photograph and SEM photographs of the 3D-printed composite ($H = 1.2 \text{ mm}$, $N = 10$, $\theta = 0^\circ/90^\circ$). The continuous black lines in Fig. 4a are CFs parallel to the X - Y plane, whereas the short black lines are CFs perpendicular to the X - Y plane. The light gray regions are PLA. The distances between the centers of two short black lines along the X - and Y -axes are approximately 1.2 and 0.5 mm, respectively, indicating that the CFs were deposited precisely by the 3D printing process. As shown in Fig. 4b, c, the CFs are composed of large quantities of CF filaments with diameters of approximately $7 \mu\text{m}$.

4.2 Controllable SE

4.2.1 Effect of the number of layers N

The SE of the composites with various N values is shown in Fig. 5. Overall, the SE increases with an increase in N ($2 \leq N \leq 10$). The increase in the SE can be attributed to an increase in the absorption attenuation SE_a , rather than an increase in SE_r , because the value of SE_r (Fig. 5b) is stable, and SE_a (Fig. 5c) increases with an increase in N ($2 \leq N \leq 10$). SE_r is stable and SE_a increases for the following reasons. Generally, SE_r is determined by the impedance mismatch between a material and air, and SE_a is determined by attenuation of electromagnetic energy, including the electric loss and polarization loss for nonmetallic composites [40]. For the composites in this work, the impedance mismatch between the material and air is due mainly to the quantity, distribution, and orientation of CFs at the surface. Large numbers of mobile charge carriers in the CFs can cause electric loss by interacting with the external E field. The interfaces between the carbon filaments and the matrix help

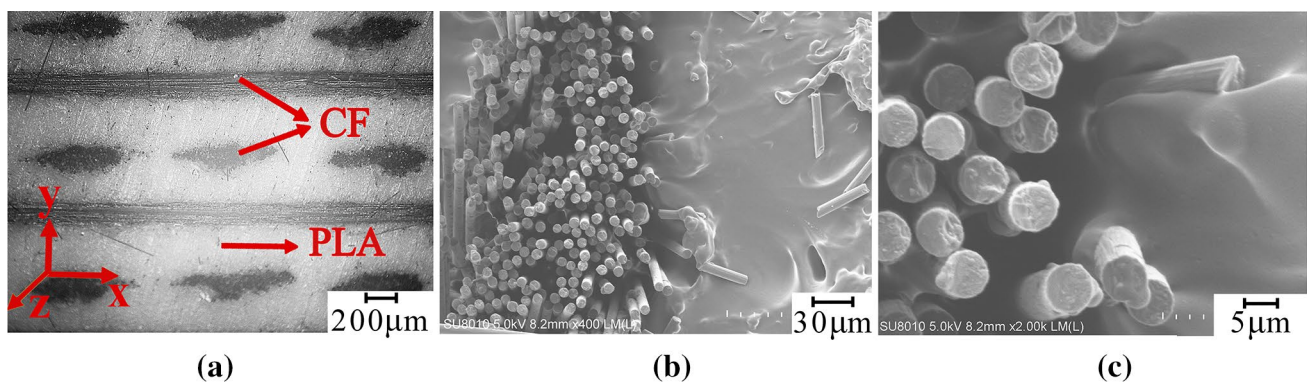
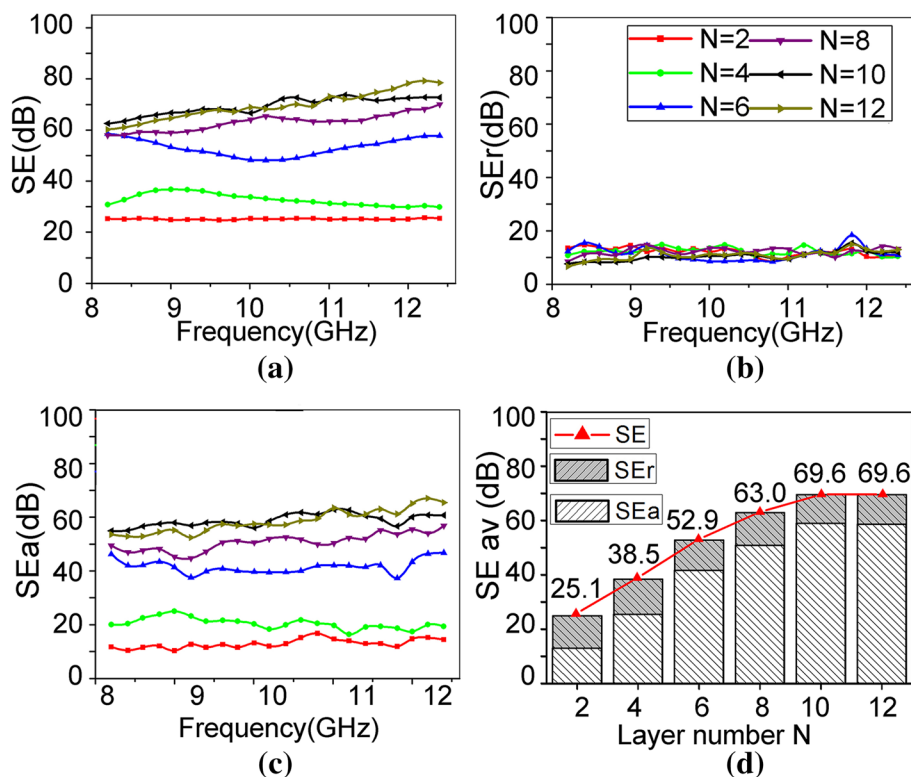


Fig. 4 a Optical microscopy image and b, c SEM photographs of composite ($H = 1.2 \text{ mm}$, $N = 10$, $\theta = 0^\circ/90^\circ$)

Fig. 5 EMIS properties of samples with various N values. **a** SE, **b** SE_r , and **c** SE_a as a function of frequency, and **d** average SE, SE_r , and SE_a as a function of N



to reflect the electromagnetic waves backward and forward many times and gradually dissipate the energy within the composites, thus causing polarization loss. The CF content of the samples in group 1 is 6.41%, and the CFs on the sample surface were all parallel to the E field, with an H value of 1.2 mm. In other words, the quantity, distribution, and orientation of the CFs at the surface were all the same. Hence, the SE_r values are almost the same. The number of mobile charge carriers contributing to electric loss and the number of interfaces between the CF and matrix contributing to polarization loss both increase with an increase in number of composite layers. Hence, SE_a is proportional to N . Consequently, a controllable SE (25.1–69.9 dB) was realized by adjusting N (2–12).

4.2.2 Effect of hatch spacing H

The SE of the composites with different H values is shown in Fig. 6. As shown in Fig. 6b, c, SE_r remained constant at approximately 10 dB, and SE_a increased from 41.2 to 64.5 dB as H decreased from 1.6 to 0.8 mm. As shown in Fig. 6d, the average SE increased from 51.1 to 75.6 dB with a decrease in H . SE_a increased with a decrease in H because the samples with smaller H had a higher CF content. The samples with H values of 1.6, 1.4, 1.2, 1.0, and 0.8 mm had CF contents of 4.81%, 5.50%, 6.41%, 7.69%, and 9.62%, respectively. With an increase in CF content, the number of free charge carriers for electric loss and the

number of interfaces for polarization loss increased. The stable SE_r indicates that H (0.8–1.6 mm) has little effect on the reflection attenuation. According to formula (4), the value of SE_r at 10 dB indicates that the samples reflect 90% of the incident electromagnetic energy and that there is a high impedance mismatch between the samples and air. Additionally, the composite exhibited a SE value above 70 dB, demonstrating the superior shielding performance of the 3D-printed composites. Thus, a controllable SE (51.1–75.6 dB) was realized by adjusting H .

4.2.3 Effect of filling angle θ

The EMIS properties of composites with different filling angles θ are shown in Fig. 7. SE, SE_r , and SE_a were all negatively correlated with θ . Specifically, as shown in Fig. 7d, when θ decreased from 90° to 0° , the average SE increased dramatically from 6.8 to 78.9 dB, SE_a increased from 4.9 to 68.3 dB, and SE_r increased from 1.9 to 10.6 dB. The reasons that SE decreased with an increase in θ are as follows. As shown in Fig. 8, the composite is located in an external E field (field density: E). The angle between the CFs and E field is θ . The E field can be decomposed into E_\perp ($E_\perp = E \cdot \sin\theta$) and E_\parallel ($E_\parallel = E \cdot \cos\theta$). Because the 1000 CF filaments in a CF bundle are separated from each other by air or the matrix, as shown in Fig. 4c, there are few conductive paths within the cross section of the CF bundle, but there is a significant conductive path along the axial direction. Thus,

Fig. 6 EMIS properties of specimens with various hatch spacing values H . **a** SE, **b** SE_r , and **c** SE_a as a function of frequency, and **d** average SE, SE_r , and SE_a as a function of hatch spacing H

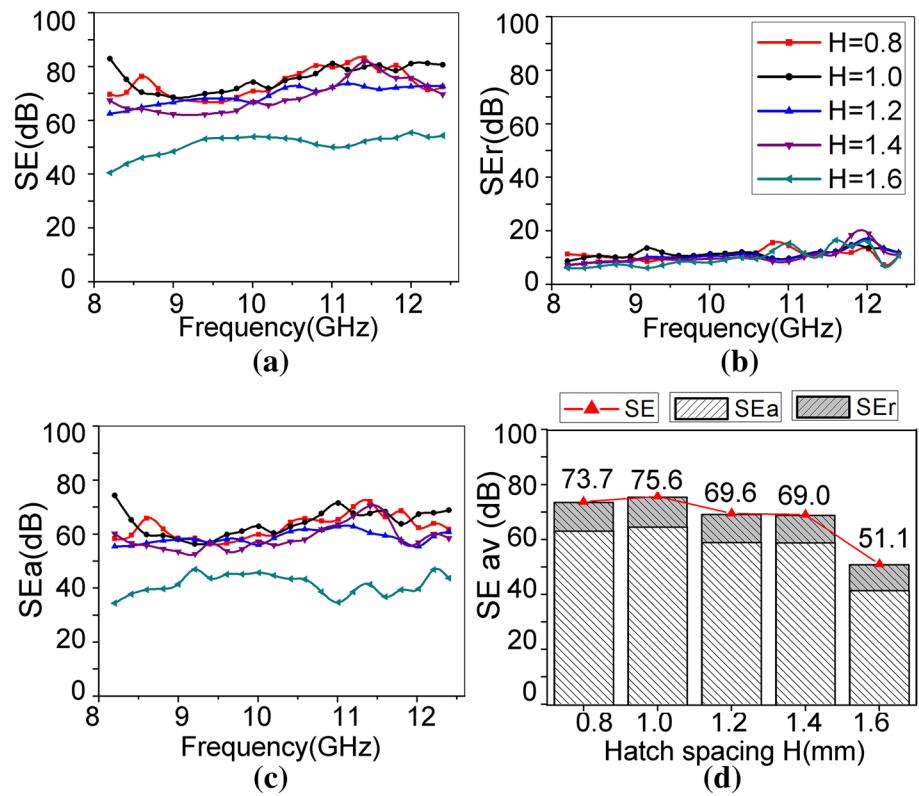
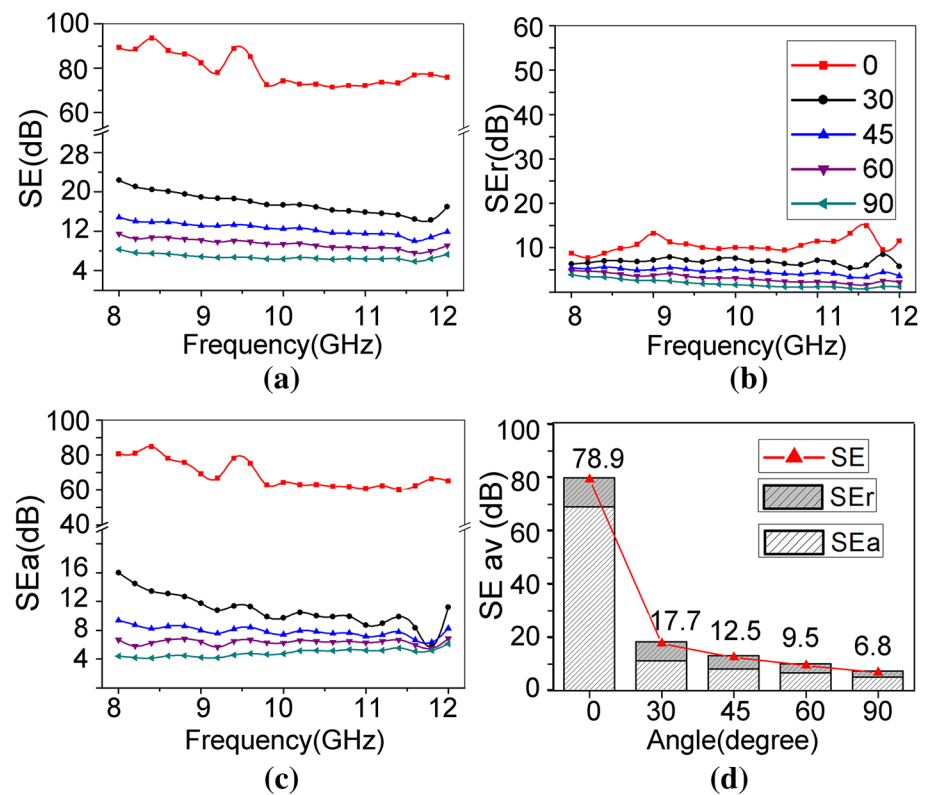


Fig. 7 EMIS properties of samples with various filling angles θ . **a** SE, **b** SE_r , and **c** SE_a as a function of frequency, and **d** average SE, SE_r , and SE_a as a function of angle θ



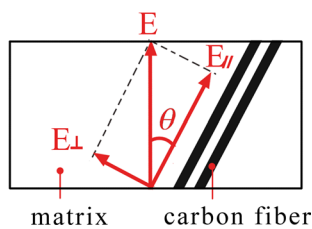


Fig. 8 Schematic diagram of E field and orientation of CF in samples

the induced current obviously flows along the axial direction of the CFs, and the current density depends mainly on $E_{||}$. The electric loss and reflection strength are positively correlated with the induced current density, which is negatively correlated with θ . Hence, SE_a and SE_r are negatively correlated with θ . Consequently, SE decreases with an increase in θ . Thus, the SE (6.8–78.9 dB) was controlled by adjusting θ (90° – 0°).

4.3 Comparison with SE reported in other studies

A comparison of our work with other studies indicates that the composites prepared by the proposed methodology are more efficient for the same thickness, as shown in Table 2. For example, the proposed composites with thicknesses of 3, 4, and 6 mm have SEs of 52.9, 63.0, and 69.6 dB, respectively, which are larger than those of previously reported composites [11, 41, 42]. Additionally, the specific SE (the ratio of the SE to the volume density) of the proposed composites is 58.6 dB cm³/g (volume density: 1.29 g/cm³), which is better than those of many other shielding materials such as metals [43] (10 dB cm³/g), CNT foams [44] (33.1 dB cm³/g), and graphene composites [45] (17–25 dB cm³/g).

4.4 SE of the shell

The SE of the shell was measured by the system shown in Fig. 9a. The system consisted of a vector network analyzer (E8363B, Agilent Technologies, USA), a shielding room

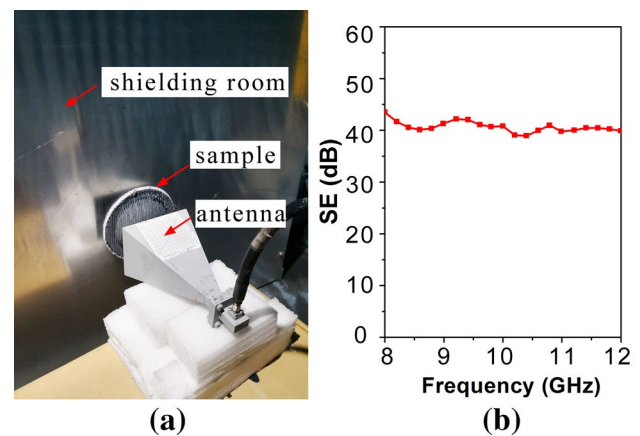


Fig. 9 **a** Photograph of the measurement facility and **b** measured SE of the hat-like shell

with dimensions of 1000 × 1000 × 1000 mm³, and transmitting and receiving X-band antennas. The center of the shell was aligned with that of the window (diameter: 100 mm) on the wall of the shielding room. The test sample was pasted on the wall using conductive glue. The transmitting antenna was inside the shielding room and transmitted the waves, and the receiver antenna was outside of the room and received the waves. The received power with no sample on the window is P_i , and the received power with samples on the window is P_t . SE of the shell equals to the ratio of P_i and P_t according to formula (5). As shown in Fig. 9b, the average value of the SE (41 dB) is close to the result in Fig. 6d (38.5 dB). Hence, the methodology can be used to fabricate shielding structures with complex geometry, such as conformal structures, which is highly significant for practical applications of the EMIS composite:

$$SE = 10 \log(P_i/P_t), \quad (5)$$

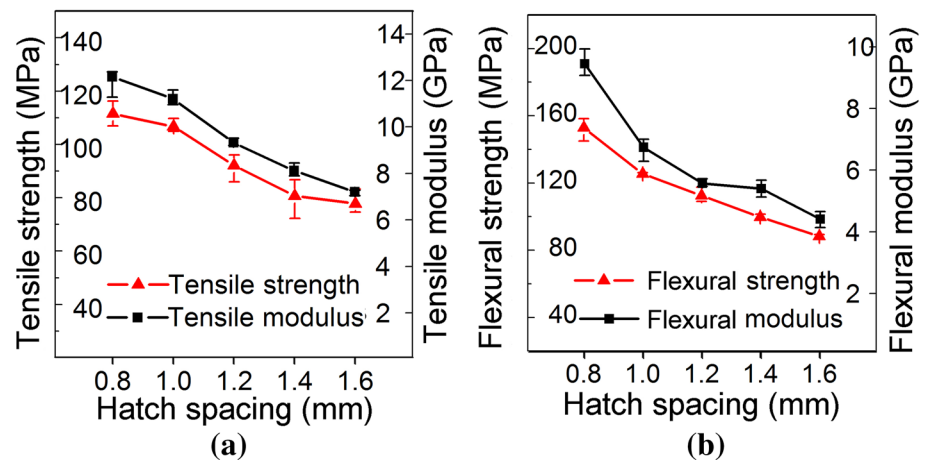
where P_i and P_t are power of the incident and transmitted electromagnetic waves.

Table 2 Comparison of SE in other studies and our work

Author	Material	Addition	Thickness (mm)	SE (dB)	References
Ameli et al.	PP-CF	10 vol%	3.2	25	[41]
Song et al.	Graphene/EVA	60 vol%	0.35	15	[38]
Hu et al.	CIP/CF/EP	0.75 wt% CIP 0.75 wt% CF	4	53.9	[11]
Wu et al.	rGO-CF/EP	0.5 wt%	6	37.6	[42]
This work	CF/PLA	9 wt%	3	52.9	–
		9 wt%	4	63.0	–
		9 wt%	6	69.6	–

EVA ethylene–vinyl acetate copolymer, rGO reduced graphene oxide

Fig. 10 **a** Tensile strength and modulus, and **b** flexural strength and modulus of the composites with N of 10 and H of 0.8 mm, 1.0 mm, 1.2 mm, 1.4 mm, and 1.6 mm



4.5 Mechanical properties

Five composites with various H values (0.8, 1.0, 1.2, 1.4, and 1.6 mm) were prepared. The CFs were configured so as to cross each other, with filling angles of 0° and 90° in adjacent layers, and N was 10. The tensile and flexural properties of the samples are shown in Fig. 10. As shown in Fig. 10a, the tensile strength increased from 77.8 to 111.0 MPa and the tensile modulus increased from 7.2 to 12.2 GPa as H decreased from 1.6 to 0.8 mm. Figure 10b shows that the flexural strength increased from 88.3 to 152.9 MPa and the flexural modulus improved from 4.4 to 9.5 GPa with a decrease in H from 1.6 to 0.8 mm. There are two reasons for the improved mechanical performance with a decrease in H . One is that the CF content increased with a decrease in H . The CF contents of the composites with H values of 0.8, 1.0, 1.2, 1.4, and 1.6 mm were 9.62%, 7.69%, 6.41%, 5.50%, and 4.81%, respectively. Another is that the interface bonding strength increased with a decrease in H . When composites with H values smaller than the diameter of the nozzle (1.5 mm) were printed, adjacent deposited lines overlapped, which resulted in contact pressure between the nozzle and the deposited lines. For example, the composites with H values of 1.4, 1.2, 1.0, and 0.8 mm had overlap widths of 0.1, 0.3, 0.5, and 0.7 mm, respectively. As H decreased, the overlap became larger, resulting in a higher contact pressure. The bonding strength of the interface between PLA and CF could be improved by the higher contact pressure. Additionally, the maximum tensile strength (111.0 MPa) and flexural strength (152.9 MPa) of the composites are much higher than those of most engineering plastics, giving the composites strong competitiveness and good potential for EMIS applications. The mechanical tests were performed on small-scale elements, so the results may be affected by the small-scale effect in some degree [46–50]. Nevertheless, we do not dive into this topic in this paper.

The maximal tensile strength in this work is better than that of most 3D-printed short-CF-reinforced composites (< 70 MPa) [31–36] and pure engineering plastics (< 50 MPa) [24–28]. The maximal flexural strength is also better than some composites and pure engineering plastics [26, 36]. However, the mechanical properties in this work are poorer than some 3D-printed continuous-CF-reinforced composites [21, 23–26]. There are two reasons. One is that the maximal CF content in this work was 9.62%, much lower than that in the other researches. Second, CFs were configured crossly in the test samples in this work, while CFs in the other researches were all oriented along the load direction.

5 Conclusions

In conclusion, a methodology for controlling the shielding properties of composites by tailoring the parameters of the 3D printing process was proposed. The results showed that the SE can be controlled in ranges of 25.1–69.9 dB, 51.1–75.6 dB, and 6.8–78.9 dB by tailoring the number of layers N (2–12), hatch spacing H (1.6–0.8 mm), and filling angle θ (90° – 0°), respectively. The mechanism of the controllability is that the content, spatial distribution, and orientation of the CFs can be flexibly and digitally controlled during the process. Additionally, the processability of complex shielding structures was demonstrated by fabrication of a CF-reinforced composite shell with a SE of 38.5 dB. The maximum tensile strength (111.0 MPa) and flexural strength (152.9 MPa) of the composites were much higher than those of most engineering plastics. Therefore, the controllable SE and superior processability and mechanical properties give the composites strong competitiveness and good potential for EMIS applications.

Acknowledgements This work was supported by the National Natural Science Foundation of China (Grant nos. 51575430 and 61671466), the National Key Research and Development Program (Grant nos. 2017YFB1103401 and 2016YFB1100902), the Rapid Manufacturing Engineering Technology Research Center of Shaanxi Province (Grant no. 2017HBGC-06), and the Innovative Talent Promotion Program-Young Science and Technology Nova Program (Grant no. 2017KJXX-14).

References

- B. Wen, X.X. Wang, W.Q. Cao, H.L. Shi, M.M. Lu, G. Wang, H.B. Jin, W.Z. Wang, J. Yuan, M.S. Cao, Reduced graphene oxides: the thinnest and most lightweight materials with highly efficient microwave attenuation performances of the carbon world. *Nanoscale* **6**(11), 5754–5761 (2014)
- R. Wang, H. Yang, J.L. Wang, F.X. Li, The electromagnetic interference shielding of silicone rubber filled with nickel coated carbon fiber. *Polym. Test.* **38**(18), 53–56 (2014)
- Y.T. Zhao, B. Wu, Y. Zhang, Y. Hao, Transparent electromagnetic shielding enclosure with CVD graphene. *Appl. Phys. Lett.* **109**(10), 103507 (2016)
- E. Enriquez, J.D. Frutos, J.F. Fernandez, M.A. Rubia, Conductive coatings with low carbon-black content by adding carbon Nanofibers. *Compos. Sci. Technol.* **93**(3), 9–16 (2014)
- Z.P. Chen, C. Xu, C.Q. Ma, W.C. Ren, H.M. Cheng, Lightweight and flexible graphene foam composites for high-performance electromagnetic interference shielding. *Adv Mater.* **25**(9), 1296–1300 (2013)
- J. Chen, J.M. Wu, H.Y. Ge, D. Zhao, C. Liu, X.F. Hong, Reduced graphene oxide deposited carbon fiber reinforced polymer composites for electromagnetic interference shielding. *Compos. Part. A Appl. Sci. Manuf.* **82**, 141–150 (2016)
- M. Mishra, A.P. Singh, V. Gupta, A. Chandra, S.K. Dhawan, Tunable EMI shielding effectiveness using new exotic carbon: polymer composites. *J. Alloy. Compd.* **688**, 399–403 (2016)
- Z. Wang, G. Wei, G.L. Zhao, Enhanced electromagnetic wave shielding effectiveness of Fe doped carbon nanotubes/epoxy composites. *Appl. Phys. Lett.* **103**(18), 183109 (2013)
- M.S. Hong, W.K. Choi, K.H. An, S.J. Kang, S.J. Park, Y.S. Lee, B.J. Kim, Electromagnetic interference shielding behaviors of carbon fibers-reinforced polypropylene matrix composites: II. Effects of filler length control. *J. Ind. Eng. Chem.* **20**(5), 3901 (2014)
- L.S. Lu, D. Xing, K.S. Teh, H.L. Liu, Y.X. Xie, X.K. Liu, Y. Tang, Structural effects in a composite nonwoven fabric on EMI shielding. *Mater. Des.* **120**, 354–362 (2017)
- T. Hu, J. Wang, J.L. Wang, R.H. Chen, Electromagnetic interference shielding properties of carbonyl iron powder-carbon fiber felt/epoxy resin composites with different layer angle. *Mater. Lett.* **142**, 242–245 (2015)
- D. Micheli, A. Vricella, R. Pastore, A. Delfini, A. Giusti, M. Albano, M. Marchetti, F. Moglie, V.M. Primiani, Ballistic and electromagnetic shielding behaviour of multifunctional Kevlar fiber reinforced epoxy composites modified by carbon. *Carbon* **104**, 141–156 (2016)
- X. Wang, M. Jiang, Z.W. Zhou, J.H. Gou, and D. Hui, 3D printing of polymer matrix composites: a review and prospective. *Compos. Part. B Eng.* **110**, 442–458 (2017)
- C.T. Huang, L.K. Shrestha, K. Ariga, S.H. Hsu, A graphene-polyurethane composite hydrogel as a potential bioink for 3D bio-printing and differentiation of neural stem cells. *J. Mater. Chem. B.* **5**, 8854–8864 (2017)
- R. Chen, J. Kang, M. Kang, H. Lee, H. Lee, Silicon pillar structure assisted three dimensional carbon nanotube assembly: fabrications and rational surface modifications. *Bull. Chem. Soc. Jpn* **91**, 979–990 (2018)
- T.D. Ngo, A. Kashani, G. Imbalzano, K.T.Q. Nguyen, D. Hui, Additive manufacturing (3D printing): a review of materials, methods, applications and challenges. *Compos. Part. B Eng.* **143**, 172–196 (2018)
- M. Sadia, B. Arafat, W. Ahmed, R.T. Forbes, M.A. Alhnan, Channelled tablets: an innovative approach to accelerating drug release from 3D printed tablets. *J. Controll. Release* **269**, 355–363 (2018)
- K. Chizari, M. Arjmand, Z. Liu, U. Sundararaj, D. Therriault, Three-dimensional printing of highly conductive polymer nanocomposites for EMI shielding applications. *Mater Today Commun.* **11**, 112–118 (2017)
- R. Kotsilkova, E. Ivanov, P. Todorov, N. Volynets, A. Paddubskaya, P. Kuzhir, V. Uglov, I. Biro, K. Kertesz, G.I. Mark, L.P. Biro, Mechanical and electromagnetic properties of 3D printed hot pressed nanocarbon/poly(lactic) acid thin films. *J. Appl. Phys.* **121**(6), 064105 (2017)
- A. Paddubskaya, N. Valynets, P. Kuzhir, K. Batrakov, S. Maksimenko, R. Kotsilkova, H. Velichkova, I. Petrova, I. Biro, K. Kertesz, G.I. Mark, Z.E. Horvath, L.P. Biro, Electromagnetic and thermal properties of three-dimensional printed multilayered nano-carbon/poly(lactic) acid structures. *J. Appl. Phys.* **119**(13), 135102 (2016)
- X.Y. Tian, T.F. Liu, C.C. Yang, D.C. Li, Interface and performance of 3D printed continuous carbon fiber reinforced PLA composites. *Compos. Part. A Appl. Sci. Manuf.* **88**, 198–205 (2016)
- X.Y. Tian, T.F. Liu, Q.R. Wang, A. Dilmurat, D.C. Li, G. Ziegmann, Recycling and remanufacturing of 3D printed continuous carbon fiber reinforced PLA composites. *J. Clean. Prod.* **142**, 1609–1618 (2017)
- F.V.D. Klift, Y. Koga, A. Todoroki, M. Ueda, Y. Hirano, R. Matsuzaki, 3D printing of continuous carbon fibre reinforced thermoplastic (CFRTP) tensile test specimens. *Open J. Compos. Mater.* **06**(01), 18–27 (2016)
- W. Hao, Y. Liu, H. Zhou, H. Chen, D. Fang, Preparation and characterization of 3D printed continuous carbon fiber reinforced thermosetting composites. *Polym Test.* **65**, 29–34 (2018)
- N. Li, Y. Li, S. Liu, Rapid prototyping of continuous carbon fiber reinforced polylactic acid composites by 3D printing. *J. Mater. Process. Technol.* **238**, 218–225 (2016)
- C. Yang, X. Tian, T. Liu, Y. Cao, D. Li, 3D printing for continuous fiber reinforced thermoplastic composites: mechanism and performance. *Rapid Prototyp. J.* **23**(1), 209–215 (2017)
- B. Safadi, R. Andrews, E.A. Grulke, Multiwalled carbon nanotube polymer composites: synthesis and characterization of thin films. *J. Appl. Polym. Sci.* **84**, 2660–2669 (2002)
- T.D. Fornes, J.W. Baur, Y. Sabba, E.L. Thomas, Morphology and properties of melt-spun polycarbonate fibers containing single- and multi-wall carbon nanotubes. *Polymer* **47**, 1704–1714 (2006)
- T. Liu, I.Y. Phang, L. Shen, S.Y. Chow, Y.D. Zhang, Morphology and mechanical properties of MWCNT reinforced nylon-6 composites. *Macromolecules* **37**, 7214–7222 (2004)
- M.L. Machado, L. Valentini, J. Biagiotti, J.M. Kenny, Thermal and mechanical properties of singlewalled carbon nanotubes-polypropylene composites prepared by melt processing. *Carbon* **43**, 1499–1505 (2005)
- L.J. Love, V. Kunc, O. Rios, C.E. Duty, A.M. Elliott, B.K. Post, R.J. Smith, C.A. Blue, The importance of carbon fiber to polymer additive manufacturing. *J. Mater. Res.* **29**(17), 1893–1898 (2014)
- H.L. Tekinalp, V. Kunc, G.M. Velez-Garcia, C.E. Duty, L. J. Love, A.K. Naskar, C.A. Blue, S. Ozcan, Highly oriented carbon fiber-polymer composites via additive manufacturing. *Compos. Sci. Technol.* **105**, 144–150 (2014)

33. F. Ning, W. Cong, J. Qiu, J. Wei, S. Wang, Additive manufacturing of carbon fiber reinforced thermoplastic composites using fused deposition modeling. *Compos. Part B* **80**, 369–378 (2015)
34. F.D. Ning, W.L. Cong, J.J. Qiu, J.H. Wei, S.R. Wang, Additive manufacturing of carbon fiber reinforced thermoplastic composites using fused deposition modeling. *Compos. Part. B Eng.* **80**, 369–378 (2015)
35. S. Jiang, Q.F. Li., Y.H. Zhao, J.W. Wang., M.Q. Kang, Effect of surface silanization of carbon fiber on mechanical properties of carbon fiber reinforced polyurethane composites. *Compos. Sci. Technol.* **110**, 87–94 (2015)
36. A. Shah, A. Ding, Y.H. Wang, L. Zhang, D.X. Wang, J. Muhammad, H. Huang, Y.P. Duan, X.L. Dong, Z.D. Zhang, Enhanced microwave absorption by arrayed carbon fibers and gradient dispersion of Fe nanoparticles in epoxy resin composites. *Carbon* **96**, 987–997 (2016)
37. Z.H. Hou, X.Y. Tian, J.K. Zhang, D.C. Li, 3D printed continuous fibre reinforced composite corrugated structure. *Compos Struct.* **184**, 1005–1010 (2018)
38. J. Song, Q. Yuan, H. Zhang, B. Huang, F. Fu, Elevated conductivity and electromagnetic interference shielding effectiveness of PVDF/PETG/carbon fiber composites through incorporating carbon black. *J Polym. Res.* **12**, 158 (2015)
39. M. Bayat, H. Yang, F.K. Ko, D. Michelson, A. Mei, Electromagnetic interference shielding effectiveness of hybrid multifunctional Fe₃O₄/carbon nanofiber composite. *Polymer* **55**, 936–943 (2014)
40. Y. Jia, K.Z. Li, L.Z. Xue, J.J. Ren, S.Y. Zhang, H.J. Li, Mechanical and electromagnetic shielding performance of carbon fiber reinforced multilayered (PyC-SiC)_n matrix composites. *Carbon* **111**, 299–308 (2017)
41. A. Ameli, P. Jung, C. Park, Electrical properties and electromagnetic interference shielding effectiveness of polypropylene/carbon fiber composite foams. *Carbon* **60**, 379–391 (2013)
42. J.M. Wu, J. Chen, Y.Y. Zhao, W.X. Liu, W.B. Zhang, Effect of electrophoretic condition on the electromagnetic interference shielding performance of reduced graphene oxide-carbon fiber/epoxy resin composites. *Compos. Part. B Eng.* **105**, 167–175 (2016)
43. Z. Chen, C. Xu, C. Ma, W. Ren, H.M. Cheng, Lightweight and flexible graphene foam composites for high-performance electromagnetic interface shielding. *Adv. Mater.* **25**, 1296–1300 (2013)
44. Y. Yang, M.C. Gupta, K.L. Dudley, R.W. Lawrence, Novel carbon nanotube polystyrene foam composites for electromagnetic interference shielding. *Nano Lett.* **5**, 2131–2134 (2005)
45. H.B. Zhang, Q. Yan, W.G. Zheng, Z. He, Z.Z. Yu, Tough graphene-polymer microcellular foams for electromagnetic interference shielding. *ACS Appl. Mater. Interfaces* **3**, 918–924 (2011)
46. A. Kausar, I. Rafique, B. Muhammad, Review of applications of polymer/carbon nanotubes and epoxy/CNT composites. *Polym. Plast. Technol.* **55**(11), 1167–1191 (2016)
47. S. Acierno, R. Barretta, R. Luciano, F.M.D. Sciarra, P. Russo, Experimental evaluations and modeling of the tensile behavior of polypropylene/single-walled carbon nanotubes fibers. *Compos. Struct.* **174**, 12–18 (2017)
48. R. Barretta, F.M.D. Sciarra, A nonlocal model for carbon nanotubes under axial loads. *Adv. Mater. Sci. Eng.* 2013, 1–6 (2013)
49. R. Barretta, M. Canadija, R. Luciano, F.M.D. Sciarra, Stress-driven modeling of nonlocal thermoelastic behavior of nanobeams. *Int. J. Eng. Sci.* **126**, 53–67 (2018)
50. M. Canadija, R. Barretta, F.M.D. Sciarra, A gradient elasticity model of BernoulliEuler nanobeams in non-isothermal environments. *Eur. J. Mech. A Solids* **55**, 243–255 (2016)

Publisher's Note Springer Nature remains neutral with regard to jurisdictional claims in published maps and institutional affiliations.